Plasmonic Hot Printing in Gold Nanoprisms

Sviatlana Viarbitskaya,*[,†] Aurélien Cuche, Alexandre Teulle, Jadab Sharma,[§] Christian Girard, Arnaud Arbouet,* and Erik Dujardin*

CEMES CNRS UPR 8011 and Université de Toulouse, 29 Rue Jeanne Marvig, BP 94347, 31055 Toulouse Cedex 4, France

S *Supporting Information*

ABSTRACT: The raster-scanned irradiation of ultrathin sub-micrometer crystalline gold colloidal prisms with the tightly focused spot of a femtosecond, near-infrared laser triggers the deterministic deformation and partial melting of nanometer-sized areas of the nanoprisms. The morphological modification of the Au nanoprisms evidences extremely localized sources of heat, the in-plane distribution of which varies with the particle shape and laser polarization. We demonstrate for the first time the direct relationship between heat source density and surface plasmon local density of states (SP-LDOS), which describes quantitatively the rich modal structure of the surface plasmons sustained by the 2D metallic platelets, independently of the knowledge of the illumination configuration. Green's Dyadic numerical simulations confirm that the optical excitation of the 2D SP modes results in the subwavelength hot imprinting of the SP modal pattern onto the metal surface.

KEYWORDS: *colloids, surface plasmon, thermoplasmonics, melting, LDOS*
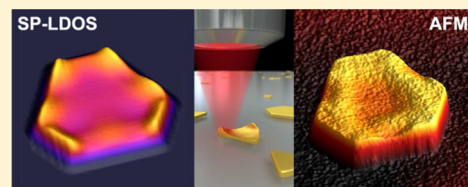
Physical properties of solid-state matter are classically related to the intrinsic concept of local density of states (LDOS) of elementary particles (electrons, photons) or excitations (phonons, plasmons). Yet, surfaces are known to markedly modify the LDOS, which provides a means to image it. For example, electron LDOS can be imaged by low-temperature scanning tunneling microscopy (STM) as it tails off into the vacuum in the vicinity of a metal−vacuum interface.[1] Similarly, photon STM was used to probe photon or electromagnetic LDOS (EM-LDOS) in the immediate proximity of dielectric and metallic nanostructures.[2] EM-LDOS, a scalar quantity, gives the only quantitative modal description of the continuous spectrum of eigenmodes in optical systems, independently of the excitation mode. For example, it appears as a constant factor in Planck's law of blackbody radiation.[3,4] Recently, EM-LDOS supported by lithographically designed metallic structures was directly imaged in the infrared range by thermal radiation STM.[5] This seminal work evidenced that realistic surfaces also sustain nonradiative (evanescent) eigenmodes that contribute to the energy storage, thereby affecting the thermal properties of metallic surfaces when the energy is subsequently released by the emission of infrared photons.[6,7] Interestingly, the interplay between optical and thermal properties in metallic surfaces has been extensively revisited in the context of plasmonics,[8] which raises the fundamental question of the relationship between thermal properties and surface plasmon LDOS (SP-LDOS).[2,9,10]

Indeed, the strong potential for subwavelength confinement and intense enhancement of the electromagnetic field in plasmonic nanostructures has fostered the interest in understanding, controlling, and exploiting the plasmon-assisted optical generation of heat at the nanometer scale.[11−13] The resonant excitation of plasmon modes produces heat that has

been imaged by photothermal microscopy techniques.[14−16] The modification of the geometrical parameters allowed tuning both the energy and anisotropy of the modes, for example in gold nanowires,[17] rod dimers,[15] particle assemblies,[18,19] diabolo[20] or G-shaped nanostructures.[21] The thermal images of these systems demonstrated that heat could be produced extremely locally, therefore opening opportunities for practical applications that require controllable nanosources of heat operated remotely by light, such as data recording,[22,23] optical manipulation,[24] catalysis,[25] cellular transfection,[26] drug delivery,[27] and therapeutic hyperthermia.[28]

From a mechanistic viewpoint, the correlation between luminescence and thermal images has established that heat production was directly linked to electromagnetic hotspots in plasmonic systems based on the calculation of electromagnetic field maps.[15,21] It is noteworthy that such a distribution of a local field results from the interaction of the plasmonic structures with the impinging field and is therefore dependent on the illumination configuration. While multiple mechanisms contribute to the SP-mediated generation of heat, high SP-induced current densities, in particular at resistive grain boundaries in polycrystalline samples, were considered as responsible for the main dissipative pathways in continuous structures.[29] Upon increasing the injected laser power, the SP-mediated thermal effects can even induce irreversible localized deformation: gold nanorods in suspension were turned into ϕ-shaped particles by pulsed laser-induced melting;[30−33] micro-bumps,[34,35] nanojets,[35,36] and nanodroplets[36] were observed in plain Au and Ni films and in lithographically defined chiral Au patterns[21,37] under femtosecond laser irradiation. Therefore, in

contrast to the pioneering work by Greffet *et al.*, in which the EM-LDOS is globally populated according to Bose−Einstein statistics by an external heating of the sample and probed locally with a near-field optical microscope,[5−7] it appears that a tightly focused, ultrashort laser pulse triggers phenomena that raise the metal temperature extremely locally over a wide tunable range from a few degrees up to complete fusion.

In this article, we show that ultrathin 2D Au crystals, subjected to a series of raster scans with a pulsed laser power exceeding an energy density threshold of 10 mJ·cm^{-2}, undergo surface modification in nanometer-scale areas. The detailed investigation of the onset of the plasmon-induced local melting by scanning electron (SEM) and atomic force microscopy (AFM) demonstrates that the fused footprint reveals the spatial distribution of the SP-LDOS with subwavelength resolution. We formally establish that the generation of heat is determined by the SP-LDOS pattern that derives from the colloidal morphology of the ultrathin Au prisms. Indeed, SP-LDOS is an intrinsic quantity that does not depend on the illumination conditions. Hence our results directly link the local heat production to designable parameters such as the colloidal shape, size, and chemical composition. This report on plasmon-mediated hot printing not only provides a direct SP-LDOS imaging technique in complex 2D structures but also opens a general way to confine heat generation at the nanoscale and even to arbitrarily select hot areas by using linearly polarized incident light that projects the SP-LDOS, hence the heat source distribution, along the polarization direction.

Micrometer large yet ultrathin (20 nm) gold prismatic platelets with well-defined triangular and truncated triangular morphologies and in-plane single-crystalline structure are synthesized as previously reported.[10] Once deposited onto a glass coverslip coated with 10 nm ITO, the sample is exposed to oxygen plasma to remove the polymer coating resulting from the synthesis (see Experimental Section for details). Individual prisms are then identified, and their morphology is characterized by recording both SEM and AFM images. The plasmon-mediated hot printing is performed by raster scanning the chosen nanoprism in the focal spot (ca. 400 nm diameter) of a linearly polarized, pulsed near-infrared laser (Figure 1a). The pulses are 150 fs at a repetition rate of 80 MHz and the wavelength is selected as 800 nm. In order to induce a moderate morphological change of the nanoprisms, the laser power is kept in the 2−2.5 mW range, as measured at the back aperture of the microscope objective, which corresponds to a fluence of 10−13 mJ·cm^{-2} at the focal point. In these conditions, the peak power density and mean value are on the order of 10^6 mW·μm^{-2} and 30 mW·μm^{-2}, respectively. After full irradiation, the same prisms are analyzed again by SEM and AFM to assess the morphological changes. By finely tuning the laser power to reach the onset of light-induced melting, we observe reproducible and polarization-dependent surface deformations by AFM imaging.

Figures 1b−d show typical examples of nanoprisms before and after undergoing a series of scans in the laser beam focal spot averaging all directions of the incident linear polarization. The platelets of different shapes but very similar sizes initially present flat and smooth single-crystalline [111] facets (Figure 1b and Figure 1d bottom). While laser irradiation with fluence in the range 1.5−4.5 mJ·cm^{-2} was shown to produce two-photon luminescence but no observable morphological alteration,[10,38] a 5- to 10-fold increase of the fluence (10−13 mJ·cm^{-2}) results in slight modifications located specifically at
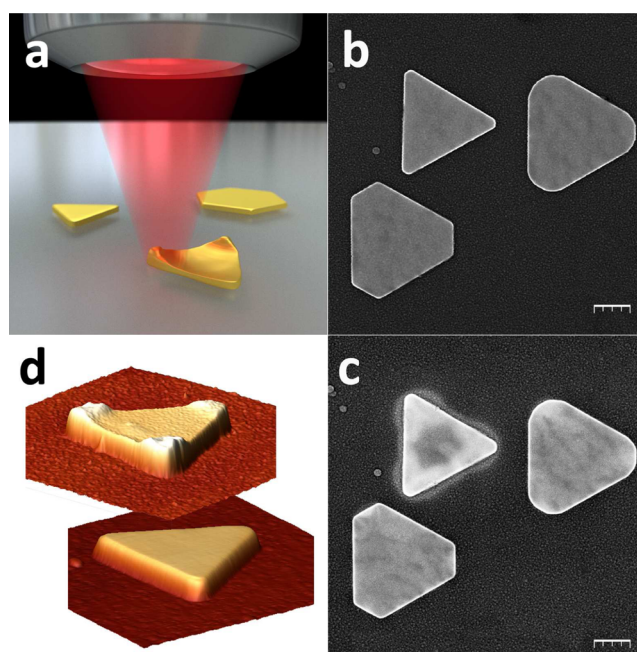

Figure 1. (a) Principle of the optical setup used for plasmon hot printing. A high numerical aperture objective is used to focus a linearly polarized 800 nm pulsed laser beam onto an ITO-coated glass coverslip bearing micrometer-sized, ultrathin Au prisms. The sample is raster scanned with an $X−Y$ piezostage. The laser fluence is limited to 10−13 mJ·cm^{-2}. The particle morphology is modified upon the laser exposure. (b, c) SEM images of a group of triangular and truncated triangular Au prism platelets (b) before and (c) after laser irradiation. The incident linearly polarized light has been successively rotated every 5° between 0° and 180° with equal irradiation time for all polarization directions. Scale bars are 200 nm. (d) 3D rendering of AFM images of a triangular prism before (bottom) and after (top) laser irradiation. The prism edge is 700 nm long, and the native thickness is 23 nm. The height perspective is identical for both top and bottom images.

the apexes and/or edges depending on the particle shape (Figure 1c and Figure 1d top). A further increase of the laser fluence beyond 15 mJ·cm^{-2} leads to severe damages (Figure S2), which renders impossible any further quantitative analysis (for details, see Section 2 in the Supporting Information).

Single linear polarization irradiations provided a deeper understanding of the corrugation emergence mechanism. Figure 2 presents SEM and AFM images of a series of triangular, truncated triangular, and hexagonal nanoprisms that have been raster scanned with a laser beam polarized along a single polarization direction, either horizontal or vertical. SEM micrographs of two triangular platelets with sharp apexes are shown before (Figures 2a and e) and after (Figures 2b and f) irradiation with horizontally and vertically polarized laser beams, respectively. Irradiation with horizontally polarized light induces a marked alteration of the two apexes along the horizontal edge of the prisms, which is visible in Figure 2b. This alteration corresponds to effective mass transport, as shown by the AFM image (Figure 2c) and profile (Figure 2d, black line). The modified apexes exhibit a 10 nm high protuberance, which represents about 50% of the initial prism thickness, while the center of the horizontal edge and the third apex retain their native thickness. This can be inferred from the height profiles shown in Figure 2d, where the black line corresponds to the profile along the edge (segment 1−2 in Figure 2c) and the red
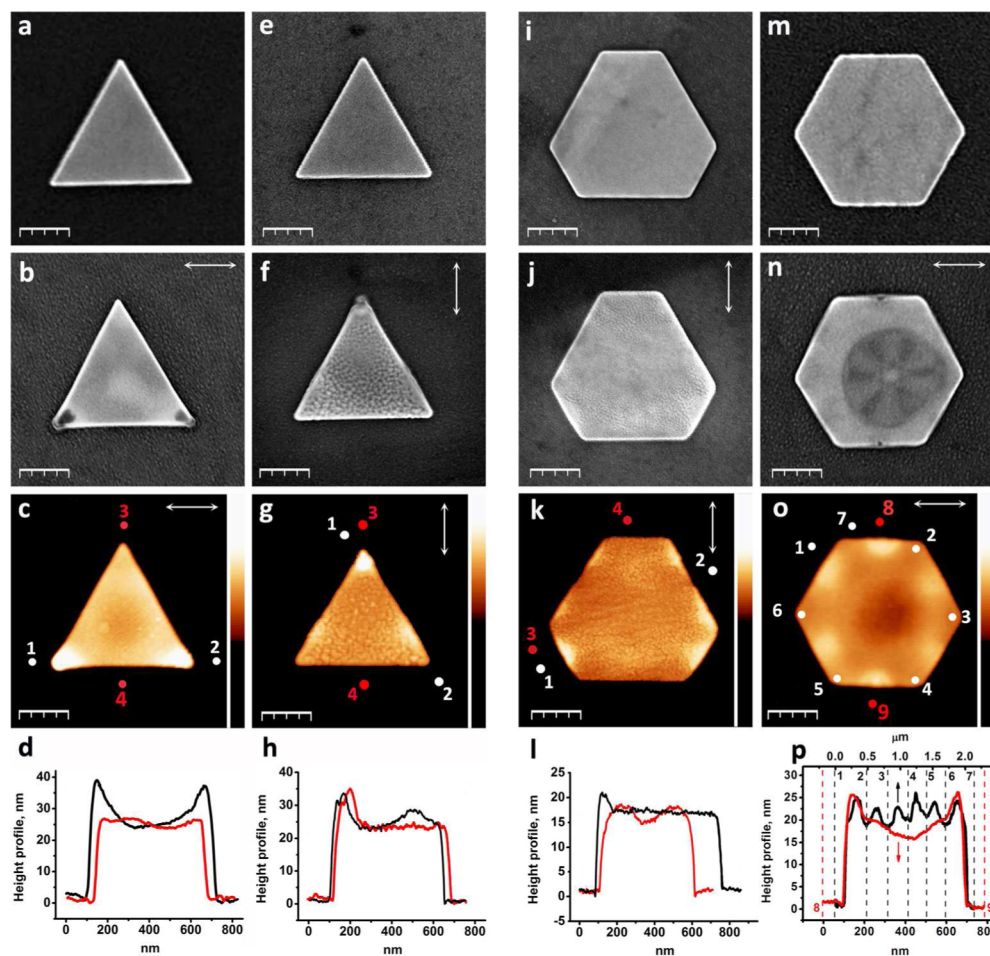
Figure 2. (a, b) SEM images of a sharp triangular Au prism (a) before and (b) after pulsed laser irradiation with a horizontally polarized laser beam. (e, f) SEM images of another Au prism (e) before and (f) after irradiation with a vertically polarized laser beam. The polarization direction is indicated by the double-headed arrows. (c, g) AFM micrographs of the Au prisms after their respective irradiation. (d, h) Height profiles along the segments 1−2 (black line) and 3−4 (red line) marked in the panels (c) and (g). (i, m) SEM images of (i) a truncated triangular and (m) a hexagonal Au prism before irradiation. (j, n) SEM images of the same Au prisms after irradiation. (k, o) AFM micrographs, corresponding to panels (j) and (n). (l, p) AFM height profiles along the segments 1−2 in (l) or 1−7 in (p) (black lines) and 3−4 in (l) or 8−9 in (p) (red lines) marked in panels (k) and (o). In (p), the black (red) dotted lines indicate the position of the white (red) markers in panel (o). Scale bars are 200 nm.

line is the profile across the center of the prism (segment 3−4 in Figure 2c). Symmetrically, the irradiation of another similar prism (Figure 2e) with vertically polarized light affects principally the upper apex (Figure 2f−h). The AFM profile extracted from Figure 2g along the 3−4 segment (Figure 2h, red line), which is parallel to the vertical polarization direction, confirms a 10 nm protrusion specifically localized at the apex. Moreover, the profile along the 1−2 line (Figure 2h, black line) evidences that the two lateral edges are also modified, albeit to a lesser extent (3−5 nm high protrusions). For both nanoprisms, the center region remains essentially featureless and forms a central low-lying plateau. The spatial distribution of laser-induced protrusions was further examined in more complex colloidal geometries such as the truncated triangular and hexagonal nanoprisms shown in Figures 2i and m. Both particles, which are of similar lateral dimensions and identical thickness, underwent irradiation with vertical and horizontal incident polarization, respectively. SEM and AFM data recorded after the irradiation (Figures 2j,k and n,o) confirm the mass transfer phenomenon. Interestingly, for these morphologies, the protrusions are located along the particle edges rather than at the apexes. The spatial distribution of the

protruding patterns respects the global symmetry of the supporting particle and polarization direction (Figures 2k and o). The truncated triangular prisms show two 3−5 nm high bumps along the longest lateral edges (Figure 2l, red curve) and a single one located at each lower truncated edge (Figure 2l, black curve). In the hexagonal prism, the protrusions are located at the middle of each edge, with a slightly stronger and more confined outcome on the two sides parallel to the incident horizontal polarization direction. Consistently, the height profile (black curve in Figure 2p) that follows the broken dashed line connecting points 1 to 7 in Figure 2o shows periodic oscillations with a slight excess of height for the 1−2 and 4−5 segments.

The morphological modifications of the 2D crystalline colloids are largely determined by the in-plane shape of the particle and the direction of the incident polarization. By combining the SEM and AFM data of the same prisms, it is also clear that the protrusions are typically 50−100 nm in diameter, irrespective of the particle shape, which is well below the nominal size of the incident laser beam (ca. 400 nm in diameter). In order to discriminate the influence of both parameters, prisms with all three shapes have undergone

multiple irradiations for which the linear polarization was successively rotated by 10° steps so that pairs of orthogonal polarization would cover all directions. The resulting nontrivial surface patterns were analyzed by AFM, as shown in Figure 3,
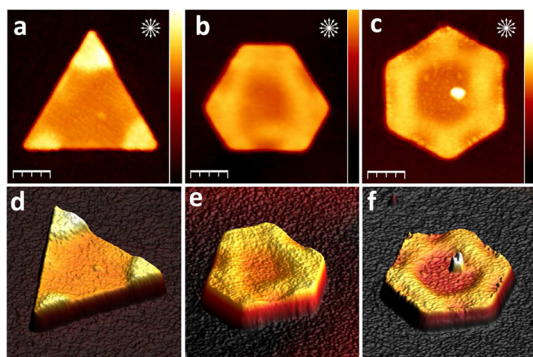

Figure 3. (a−c) AFM images of (a) triangular, (b) truncated triangular, and (c) hexagonal Au prisms after a series of irradiation with a tightly focused 800 nm laser beam. For each successive scan the polarization was rotated by 10 degrees, simulating the irradiation with a circularly polarized laser beam. The small but high central feature in (c) is an adventitious dirt particle that contaminated the sample after irradiation and did not result from the hot printing process. (d−f) 3D rendering of AFM images in panels (a)−(c), respectively. Scale bars are 200 nm.

and clearly possess similar symmetries to their corresponding supporting particles. The protruding areas are primarily located along symmetrical arrowhead patterns at the apexes of the sharp triangle (Figures 3a,d), whereas they are found near the apexes of the truncated triangle and of the hexagon with elevated interconnecting regions (Figures 3b,c,e,f). All three types of prisms show a seemingly unperturbed flat central area after irradiation.

Tapping-mode AFM phase images of irradiated prisms present a uniform contrast, including in the areas of protrusion (Figure S3). The uniform dissipation signal confirms the absence of remaining organic adsorbate following the O_2 plasma treatment that would be locally modified during irradiation. Rather, it strongly suggests that the protuberances are made of gold and that the morphology modifications result from the melting in extremely localized regions of the prisms that vary with the incident polarization. Yet, the intriguing patterning cannot be accounted for by the sole action of laser-induced melting since each and every pixel in the raster-scanned area is exposed to the same laser irradiation.

The bulges and localized melting areas along the platelet apexes and edges in Figures 2 and 3 strikingly resemble the two-photon luminescence (TPL) patterns observed at much lower fluence (see also Section 1 in the Supporting Information).[10] In this earlier work, we have established that the TPL signal was directly related to the squared projected distribution of SP-LDOS. In the following, we present a model that explicitly relates the heat source density to the surface plasmon local density of states, which represents the number of surface electromagnetic modes per unit energy at a given location. Accordingly, we demonstrate that the heat distribution induced by the laser in the gold prisms is strictly proportional to the partial SP-LDOS in the plane of the prisms (see Supporting Information for full derivation). When the incident Gaussian laser beam is located at the position $\mathbf{R_0}$ in the particle,

the heat generated locally at $\mathbf{R_0}$, $Q(\mathbf{R_0}, \omega_0)$ is related to the local electric field $E(\mathbf{R_0}, \mathbf{r}, \omega_0)$ as follows:[15]

$$Q(\mathbf{R_0}, \omega_0) = \frac{\omega_0}{8\pi} \varepsilon_m''(\omega_0) \int_V |E(\mathbf{R_0}, \mathbf{r}, \omega_0)|^2 \, d\mathbf{r} \qquad (1)$$

in CGS units, where ω_0 is the angular frequency of the incident light beam and ε_m'' is the imaginary part of the dielectric function of the metal. Moreover, for thin metallic platelets illuminated with a circularly polarized plane wave in normal incidence, we have demonstrated, in ref 10, that the intensity of the local electric field could be related to the product of the incident intensity and the in-plane component of the full SP-LDOS, $\rho_\parallel(\mathbf{r})$:

$$|E(\mathbf{R_0}, \mathbf{r}, \omega_0)|^2 \sim |E_0(\mathbf{R_0}, \mathbf{r}, \omega_0)|^2 \rho_\parallel(\mathbf{r}, \omega_0) \qquad (2)$$

Hence,

$$Q(\mathbf{R_0}, \omega_0) = \frac{3\pi c^3}{8\omega_0} \varepsilon_m''(\omega_0) \int_V |E_0(\mathbf{R_0}, \mathbf{r}, \omega_0)|^2 \rho_\parallel(\mathbf{r}, \omega_0) \, d\mathbf{r} \qquad (3)$$

where c is the light speed. When the incident light is linearly rather than circularly polarized, $\rho_\parallel(\mathbf{r})$ in eq 3 is replaced by the partial SP-LDOS, its projection along the polarization direction. It therefore appears that the heat distribution can be finely modulated in the plane of the 2D Au prisms. For example, in the sequential illumination illustrated in Figure 3, the full in-plane SP-LDOS is probed through the accumulation of orthogonal projections onto the polarization direction.[39] When the SP-LDOS of a sharp triangle similar to the one displayed in Figure 2 is projected along a single horizontal polarization direction, it presents two intense maxima at the two apexes along the horizontal edge, with weaker features along the edges (Figure 4a). The projection along the vertical polarization results in a single dominant spot at the upper apex (Figure 4b). The AFM topography images in Figures 4d and e clearly show that the areas of highest protuberances precisely match those of the most intense SP-LDOS. Even the secondary features coincide satisfactorily. Similarly, Figure 4c confirms that the partial SP-LDOS along the vertical polarization associated with a truncated triangle isomorph to the one studied in Figure 2 closely matches the AFM topographical patterns shown in Figure 4f. This striking correspondence appears all the more clearly when the AFM height data are plotted with a highly contrasting height color scale, which is further emphasized by thresholding the SP-LDOS maps at ca. 50−60% and above 75%. In so doing, Figures 4a, b, and c yield the corresponding Figures 4g, h, and i, which further evidences that the mass transport observed by AFM is triggered by the plasmonic properties of the Au platelets but also suggests that the strongly localized melting results from a highly nonlinear mechanism.

Pulsed laser-induced modifications in ultrathin gold films involve extremely complex effects, including film deformation and metal melt hydrodynamics, which may differ when tuning the pulse width from nano- to femtoseconds.[40−42] In particular, Au films melt extremely locally (ca. 100 nm) at reduced laser fluence when using shorter pulses, rather than undergoing disruptive ablation.[35,36,43−46] For 100 fs laser irradiations at UV wavelength, typically 400 nm, the onset fluence for melting is about 10−100 mJ·cm^{-2} depending on the thickness, purity, and support of the Au film.[13,42,47−49] The energy absorbed by the colloidal platelets from the 10−13 mJ·cm^{-2} laser beam used in
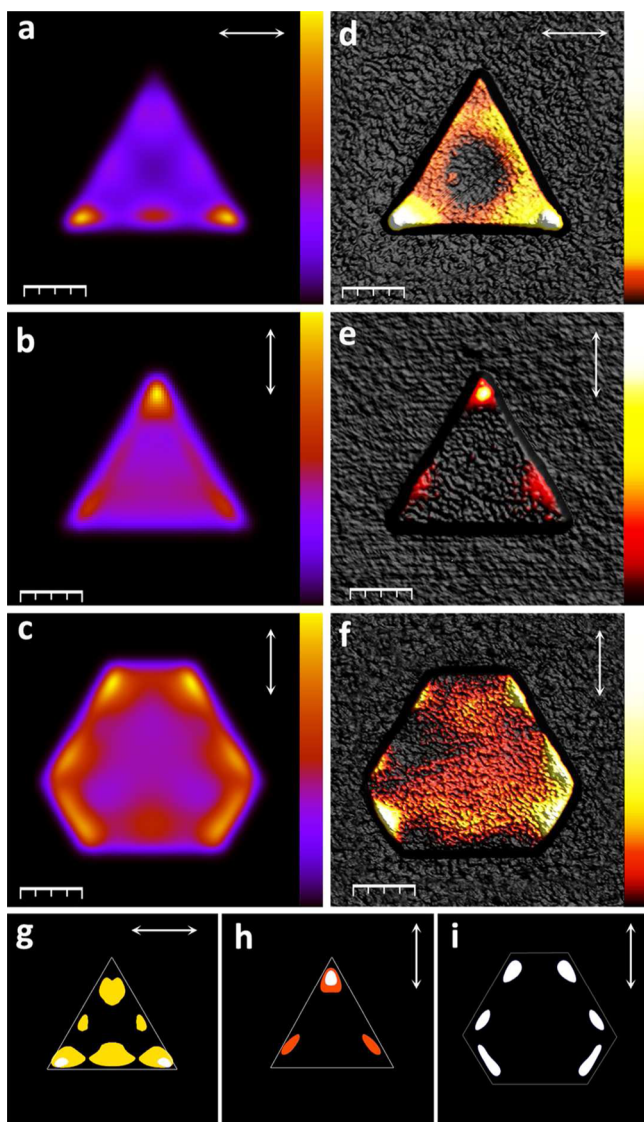
Figure 4. (a−c) Calculated partial SP-LDOS of (a, b) triangular and (c) truncated platelets projected along the direction shown by the double-headed arrows. The excitation wavelength is 800 nm. Each SP-LDOS map is normalized to its maximal value. (d−f) AFM images of prisms after irradiations at 800 nm. Laser polarization directions are indicated by the white double-headed arrows. (g−i) Thresholded calculated partial SP-LDOS from the panels (a)−(c), respectively. In (g) the yellow color depicts regions where the normalized partial SP-LDOS in panel (a) exceeds 50%. In (h), orange shows the areas in (b) where the normalized SP-LDOS exceeds 60%. In (g)−(i), white areas correspond to a normalized SP-LDOS exceeding 75% in (a)−(c). Scale bars are 200 nm.

excitation pulse, a very effective electron−phonon energy transfer prevails initially (with a characteristic time scale of ∼10 ps),[49,52] which eventually leads to a significant elevation of the lattice temperature. As a result, the fusion threshold is locally overcome and induces Au melting in restricted areas. However, it has been shown that this initial energy transfer is followed by subsequent exchanges between electrons and phonons.[45] During this mutual energy exchange, the maximum temperature of the hot electrons decreases rapidly, which also leads to a rapid loss of electron−phonon coupling so that the final thermalization of the entire prism volume occurs close to but below the melting temperature.[49] In the transient nonlinear regime reached at electronic temperatures exceeding about 5000 K, both the electronic heat capacity and the electron−phonon coupling factor depend directly on the electronic DOS.[47,48,51] The SP-LDOS therefore provides supplementary states in which more hot electrons can be generated by the collective excitation of surface plasmon modes. Remarkably, this extra energy input channel is spatially patterned since the SP-LDOS of the nanoprisms has a contrasted 2D spatial distribution. This conjunction of locally confined, nonlinear melting processes under femtosecond excitation with in-plane patterning of the plasmon modal distribution is directly illustrated by the striking similarity between the patterns of high SP-LDOS and the AFM images in Figure 4, which strongly suggests that the melting onset is overcome only in areas where the SP-LDOS is significant. Here, we experimentally and formally demonstrate the direct link between the laser-induced hot printing in gold nanostructures and the SP-LDOS, which is an intrinsic property of the particle. Importantly, our results bring a deeper understanding to the recent phenomenological association of laser-induced formation of protrusions with electromagnetic hotspots in plasmonic structures.[21,37] Indeed, depending on the laser fluence, focal spot diameter, and film extension, protrusions with different morphologies and characteristic sizes such as microbumps[34,45] and liquid nanojets[21,43] have been reproducibly observed under femto-second laser pulse irradiation. Their formation mechanisms are still largely debated,[21,35,49] but a consensual view is that the transient melting and the associated relaxation of the initial compressive stress result in the local upward acceleration of the molten gold and the formation of the protrusion at the center of the laser spot. It should be pointed out that microbumps formed by the plastic deformation (buckling) have a typical diameter that exceeds 0.5 μm,[35,43,44] which is much larger than the features observed in our experiments. On the contrary, liquid metal droplets can be as small as a few tens of nanometers in diameter,[21,36,43] in agreement with the observed patterns. Moreover, the high surface tension of liquid gold would reinforce the formation of bulging spherical caps of liquid gold at the focal spot. The liquid gold is surrounded by an area of softened metal where mass transport occurs under the driving force of the surface tension of the liquid zone. After accumulation of successive raster scans, the net mass transport is from the areas where the SP-LDOS is minimal, as the melting threshold was never overcome, toward areas where the SP-LDOS is maximal. The origin of the matter brought into the protrusions is further answered by a more careful observation of the nanoprisms after irradiation. As an example, Figure 2n shows that the initially uniform SEM contrast reveals a 6-fold symmetrical pattern in a large central area of the hexagonal prism (see also Figure S2c). This area corresponds to a large depression area seen in the AFM image (Figure 2o) and cross

this work is therefore significantly smaller than the energy required to directly melt the Au platelets, all the more so as the imaginary part of the dielectric function of gold is markedly lower at a wavelength of 800 nm, used here, compared to the UV range.[50] The subfusion conditions are experimentally attested by the intact in-plane shape of the irradiated colloids. Yet the 150 fs laser pulses generate extremely hot electrons with a typical peak electronic temperature of 6500 K (see details in the Supporting Information) that brings Au films in a nonlinear regime where both the electron heat capacity and the electron−phonon coupling factor are significantly reinforced compared to their room-temperature values.[47,48,51] After the

section (Figure 2p, red curve). In AFM, the depression area is smooth and does not exhibit a similar 6-fold symmetrical corrugation. In pristine prisms, the secondary electrons generated by the 20 kV incident beam emerge from a typical depth of 10 nm or less and so originate from the uppermost twin single crystal. Irrespective of the location in the prism, the secondary electrons travel through the same environment and create a uniform contrast. As the plasmon-induced topographical pattern formation proceeds by mass transport toward the peripheral, 10 nm high protrusions, a central area of the upper single crystal is significantly thinned down (the prisms' total thickness decreases from an initial 19−20 to 14 nm in the depleted area). When imaging the prism after laser irradiation, in the same SEM imaging conditions, the in-lens detected secondary electrons also originate from the lowermost twin crystal and travel through the uppermost one. One possible explanation of the observed contrast is that the electrons experience the atom density moiré patterns caused by minute rotational and/or translational misalignment of the two twins. Alternatively, the secondary electrons may also emerge from the region between the prism and the underlying ITO and therefore carry interfacial information that would result in the contrast formation. In either case, the observations are consistent with the formation of the depleted area at the center of the prisms.

The moderate hot printing does not modify the 2D geometrical outline of the prisms, which essentially preserves their initial in-plane shape. Consequently, the in-plane SP-LDOS, $\rho_\parallel$, is not modified during the laser irradiation, the effect of which can be cumulated by the successive addition of pulses (Figure 3). This is confirmed by the TPL mapping that is related to $\rho_\parallel$ and that shows very marginal alteration unless severe damage occurs (e.g., when fluence exceeds 15 mJ·cm^{-2}). In contrast, the plasmon-induced hot printing does modify the local thickness of the platelets, which should reflect on the z component of the SP-LDOS, ρ_z. Unlike TPL, other techniques such as electron energy loss spectroscopy, which are essentially sensitive to ρ_z,[53−55] would be able to probe this SP-LDOS self-induced engineering.

In summary, plasmon-mediated, local melting under pulsed laser irradiation has recently emerged as a new imaging technique capable of directly resolving the plasmonic properties of complex planar metallic nanostructures that were so far associated with areas of high electric field or high current areas. As a thermal imaging technique, it relies on a local probe and offers an extremely high resolution with spectral tunability unlike fluorescence polarization anisotropy or thermal radiation STM. Here, we have demonstrated for the first time both experimentally and theoretically the direct link between the local generation of heat in the metal under pulsed laser irradiation in plasmonic nanostructures and the SP-LDOS, which is an intrinsic property of the irradiated object, irrespective of the illumination conditions. When using 100−200 fs laser pulses, a deeply subwavelength resolution ($\sim \lambda/10$) is achieved through a nonlinear thermoplastic mechanism that needs further investigations. Thus, SP-induced hot printing can be conceived as a highly resolved SP-LDOS imaging method, the implementation of which is much more straightforward than fluorescence lifetime microscopy or EELS. Moreover, SP-LDOS controls a large number of properties in and near metallic structures such as luminescence, emission, electron−plasmon interaction, field confinement, and enhancement. Our direct and detailed imaging technique will be beneficial for the

design of new multifunctional or transductive modal plasmonic devices. Beyond mere SP-LDOS imaging, the engineering of the modal distribution of plasmons opens a general way to confine heat generation at the nanoscale. Indeed our earlier work has demonstrated that SP-LDOS can be modulated by shaping 2D crystalline colloids[38] or by tuning the interparticle coupling.[10,56] In particular, the ultrathin single-crystalline prisms with lateral sizes comparable to the optical wavelength studied in this work exhibit a very well-defined in-plane distribution of higher order modes associated with resonances in the technologically relevant near-IR region. The projection of the SP-LDOS by using linearly polarized light provides for a way to arbitrarily select the areas where heat is generated and hence to control the planar heat source distribution. Finally, in the studied systems, the in-plane partial SP-LDOS, $\rho_\parallel$, determines the regions where temperatures capable of inducing morphological changes are reached, but this perturbation mostly affects the out-of-plane partial SP-LDOS, ρ_z. Thus, the plasmon-mediated hot printing in planar plasmonic structures could be advantageously exploited to fine-tune the SP-LDOS with a 100 nm spatial resolution. Such a general leverage of the thermo-optical properties at the nanoscale can be of great practical interest in emerging fields such as nanopatterning, nanochemistry, nanofluidics, and nanomedicine.

■ EXPERIMENTAL SECTION

Sample Preparation. Gold nanoprisms with lateral sizes ranging between 500 and 1000 and 20 nm average thickness were prepared by a quantitative one-pot synthesis, the protocol of which is described elsewhere.[10] The prisms are composed of two superimposed single crystals sharing a 2D twin boundary along the {111} zone axis and that extend laterally over the entire prisms (data not shown). The colloids were drop-casted for 5 min before immersing the cross-marked substrate in a warm water bath for 2 min with gentle stirring. Organic adsorbates were removed just before performing experiments by three successive 5 min oxygen plasma cleanings separated by 5 min cooling time under vacuum. Scanning electron microscopy (Zeiss 1540XB) and atomic force microscopy (Dimension 3000 Veeco-Bruker) were performed to identify individual prisms to be studied and measure their dimensions. SEM and AFM measurements were again performed after particle irradiation to visualize the modified morphology. AFM images were processed with the WSxM software.[57]

Plasmon Hot Printing. Sample illumination was carried out using a TPL scanning microscopy setup.[10] The schematic of the experiments is shown in Figure 1a. The linearly polarized beam of a Ti:sapphire femtosecond laser (Coherent Chameleon Ultra II) delivering 150 fs near-infrared pulses tunable between 680 and 1080 nm at a repetition rate of 80 MHz was focused onto the sample in a home-built optical microscope objective. The linear polarization direction of the incident light was controlled by a $\lambda/2$ plate (Thorlabs AHWP05M-980). The laser beam was modulated with an optical chopper at 6 kHz to allow lock-in detection of the TPL signal. TPL was collected in an epi-collection geometry, separated from the excitation beam by a dichroic mirror (Semrock, FF665-Di02), and focused on a photomultiplier tube (PMT; Hamamatsu H7422P-40) operated in analogue mode. The TPL maps were obtained by raster scanning the sample with a high precision $X-Y$ piezostage (Mad City Laboratories NanoPDQ250) controlled by a homemade LabView program.

Full irradiations consisted in a series of 10 raster scans with air objective (Olympus 100×, NA 0.8) for particles reported in Figures 2, 4, and S2a−f. Twenty raster scans with an oil immersion objective (Olympus 100×, NA 1.4), approached from the substrate side, were performed on particles in Figures 1, 3, and S2h,g. The average scanning speed was 350 nm/s, the scan step in the X and Y directions was $d = 55$ nm, and the pixel dwell time was 150 ms. The pixel size is defined by the scan step size and corresponds to d^2. For each scan, the total average laser exposure time per pixel was 40 μs and the average number of pulses delivered per pixel was 3×10^6. The laser power range used with the oil immersion objective was kept in the range to obtain a low fluence at the sample plane, ca. $1-4$ mJ·cm^{-2}. Both objectives induced comparable morphological changes, and the choice of one or another was dictated by the desired resolution of the corresponding TPL maps.

ASSOCIATED CONTENT

Ⓢ Supporting Information

Supporting Information contains (1) TPL vs hot printing and near-field intensity vs SP-LDOS comparison; (2) high laser fluence effects; (3) AFM phase imaging of Au prisms after laser irradiation; (4) theoretical derivation of the relationship between heat distribution and SP-LDOS in two-dimensional plasmonic systems; (5) expression of the power dependence; (6) calculation of the temperature increase using the two-temperature model. The Supporting Information is available free of charge on the ACS Publications website at DOI: 10.1021/acsphotonics.5b00100.

AUTHOR INFORMATION

Corresponding Authors
*E-mail: sviatlana.viarbitskaya@gmail.com.
*E-mail: arbouet@cemes.fr.
*E-mail: dujardin@cemes.fr.

Present Addresses
†Laboratoire Interdisciplinaire Carnot de Bourgogne CNRS-UMR 6303, Université de Bourgogne, 21078 Dijon, France.
§Centre for Nano Science and Nano Technology, Panjab University, Chandigarh-160014, Chandigarh, India.

Author Contributions
S.V., A.A., C.G., and E.D. conceived the experiments. J.S. synthesized the Au prisms. S.V. prepared the samples and performed the structural characterization (SEM, AFM). S.V. and A.C. performed the pulsed laser experiments. S.V. processed the data. C.G., A.T., and S.V. performed GDM calculations. S.V., E.D., A.A., C.G., and A.C. analyzed the results. All coauthors contributed to the writing of the article.

Notes
The authors declare no competing financial interest.

ACKNOWLEDGMENTS

REFERENCES

(1) Crommie, M. F.; Lutz, C. P.; Eigler, D. M. Confinement of electrons to quantum corrals on a metal surface. *Science* **1993**, *262*, 218−220.

(2) Chicanne, C.; David, T.; Quidant, R.; Weeber, J. C.; Lacroute, Y.; Bourillot, E.; Dereux, A.; des Francs, G. C.; Girard, C. Imaging the local density of states of optical corrals. *Phys. Rev. Lett.* **2002**, *88*, 097402.

(3) Landau, L. D.; Lifshitz, E. M. *Statistical Physics*, 3rd ed.; Pergamon: London, 1960.

(4) Loudon, R. *The Quantum Theory of Light.*, 3rd ed.; Oxford University Press: London, 2000.

(5) De Wilde, Y.; Formanek, F.; Carminati, R.; Gralak, B.; Lemoine, P.-A.; Joulain, K.; Mulet, J.-P.; Chen, Y.; Greffet, J.-J. Thermal radiation scanning tunnelling microscopy. *Nature* **2006**, *444*, 740−743.

(6) Carminati, R.; Greffet, J. J. Near-field effects in spatial coherence of thermal sources. *Phys. Rev. Lett.* **1999**, *82*, 1660−1663.

(7) Greffet, J. J.; Carminati, R.; Joulain, K.; Mulet, J. P.; Mainguy, S. P.; Chen, Y. Coherent emission of light by thermal sources. *Nature* **2002**, *416*, 61−64.

(8) Baffou, G.; Quidant, R. Thermo-plasmonics: using metallic nanostructures as nano-sources of heat. *Laser Photonics Rev.* **2012**, *7*, 171−187.

(9) Girard, C.; Dujardin, E. Near-field optical properties of top-down and bottom-up nanostructures. *J. Opt. A: Pure Appl. Opt.* **2006**, *8*, S73−S86.

(10) Viarbitskaya, S.; Teulle, A.; Marty, R.; Sharma, J.; Girard, C.; Arbouet, A.; Dujardin, E. Tailoring and imaging the plasmonic local density of states in crystalline nanoprisms. *Nat. Mater.* **2013**, *12*, 426−432.

(11) Link, S.; Burda, C.; Nikoobakht, B.; El-Sayed, M. A. Laser-induced shape changes of colloidal gold nanorods using femtosecond and nanosecond laser pulses. *J. Phys. Chem. B* **2000**, *104*, 6152−6163.

(12) Govorov, A. O.; Richardson, H. H. Generating heat with metal nanoparticles. *Nano Today* **2007**, *2*, 30−38.

(13) Hashimoto, S.; Werner, D.; Uwada, T. Studies on the interaction of pulsed lasers with plasmonic gold nanoparticles toward light manipulation, heat management, and nanofabrication. *J. Photochem. Photobiol. C* **2012**, *13*, 28−54.

(14) Berciaud, S.; Cognet, L.; Blab, G. A.; Lounis, B. Photothermal heterodyne imaging of individual nonfluorescent nanoclusters and nanocrystals. *Phys. Rev. Lett.* **2004**, *93*, 257402.

(15) Baffou, G.; Girard, C.; Quidant, R. Mapping heat origin in plasmonic structures. *Phys. Rev. Lett.* **2010**, *104*, 136805.

(16) Desiatov, B.; Goykhman, I.; Levy, U. Direct temperature mapping of nanoscale plasmonic devices. *Nano Lett.* **2014**, *14*, 648−652.

(17) Baffou, G.; Kreuzer, M. P.; Kulzer, F.; Quidant, R. Temperature mapping near plasmonic nanostructures using fluorescence polarization anisotropy. *Opt. Express* **2009**, *17*, 3291−3298.

(18) Sanchot, A.; Baffou, G.; Marty, R.; Arbouet, A.; Quidant, R.; Girard, C.; Dujardin, E. Plasmonic nanoparticle networks for light and heat concentration. *ACS Nano* **2012**, *6*, 3434−3440.

(19) Govorov, A. O.; Zhang, W.; Skeini, T.; Richardson, H.; Lee, J.; Kotov, N. A. Gold nanoparticle ensembles as heaters and actuators: melting and collective plasmon resonances. *Nanoscale Res. Lett.* **2006**, *1*, 84−90.

(20) Coppens, Z. J.; Li, W.; Walker, D. G.; Valentine, J. G. Probing and controlling photothermal heat generation in plasmonic nanostructures. *Nano Lett.* **2013**, *13*, 1023−1028.

(21) Valev, V. K.; Denkova, D.; Zheng, X.; Kuznetsov, A. I.; Reinhardt, C.; Chichkov, B. N.; Tsutsumanova, G.; Osley, E. J.; Petkov, V.; De Clercq, B.; Silhanek, A. V.; Jeyaram, Y.; Volskiy, V.; Warburton, P. A.; Vandenbosch, G. A. E.; Russev, S.; Aktsipetrov, O. A.; Ameloot, M.; Moshchalkov, V. V.; Verbiest, T. Plasmon-enhanced sub-wavelength laser ablation: plasmonic nanojets. *Adv. Mater.* **2012**, *24*, OP29−OP35.

(22) Zijlstra, P.; Chon, J. W. M.; Gu, M. Five-dimensional optical recording mediated by surface plasmons in gold nanorods. *Nature* 2009, *459*, 410−413.

(23) Stipe, B. C.; Strand, T. C.; Poon, C. C.; Balamane, H.; Boone, T. D.; Katine, J. A.; Li, J. L.; Rawat, V.; Nemoto, H.; Hirotsune, A.; Hellwig, O.; Ruiz, R.; Dobisz, E.; Kercher, D. S.; Robertson, N.; Albrecht, T. R.; Terris, B. D. Magnetic recording at 1.5 Pb m(−2) using an integrated plasmonic antenna. *Nat. Photonics* 2010, *4*, 484−488.

(24) Cuche, A.; Canaguier-Durand, A.; Devaux, E.; Hutchison, J. A.; Genet, C.; Ebbesen, T. W. Sorting nanoparticles with intertwined plasmonic and thermo-hydrodynamical forces. *Nano Lett.* 2013, *13*, 4230−4235.

(25) Cao, L.; Barsic, D. N.; Guichard, A. R.; Brongersma, M. L. Plasmon-assisted local temperature control to pattern individual semiconductor nanowires and carbon nanotubes. *Nano Lett.* 2007, *7*, 3523−3527.

(26) Urban, A. S.; Pfeiffer, T.; Fedoruk, M.; Lutich, A. A.; Feldmann, J. Single-step injection of gold nanoparticles through phospholipid membranes. *ACS Nano* 2011, *5*, 3585−3590.

(27) Timko, B. P.; Dvir, T.; Kohane, D. S. Remotely triggerable drug delivery systems. *Adv. Mater.* 2010, *22*, 4925−4943.

(28) Huang, X.; Jain, P. K.; El-Sayed, I. H.; El-Sayed, M. A. Plasmonic photothermal therapy (PPTT) using gold nanoparticles. *Lasers Med. Sci.* 2008, *23*, 217−228.

(29) Baffou, G.; Quidant, R.; Girard, C. Heat generation in plasmonic nanostructures: Influence of morphology. *Appl. Phys. Lett.* 2009, *94*, 153109.

(30) Link, S.; Burda, C.; Wang, Z. L.; El-Sayed, M. A. Electron dynamics in gold and gold-silver alloy nanoparticles: The influence of a nonequilibrium electron distribution and the size dependence of the electron-phonon relaxation. *J. Chem. Phys.* 1999, *111*, 1255−1264.

(31) Link, S.; Burda, C.; Nikoobakht, B.; El-Sayed, M. A. Laser-induced shape changes of colloidal gold nanorods using femtosecond and nanosecond laser pulses. *J. Phys. Chem. B* 2000, *104*, 6152−6163.

(32) Imura, K.; Okamoto, H. Ultrafast photoinduced changes of eigenfunctions of localized plasmon modes in gold nanorods. *Phys. Rev. B* 2008, *77*, 041401.

(33) Kuhlicke, A.; Schietinger, S.; Matyssek, C.; Busch, K.; Benson, O. In situ observation of plasmon tuning in a single gold nanoparticle during controlled melting. *Nano Lett.* 2013, *13*, 2041−2046.

(34) Valev, V. K.; Libaers, W.; Zywietz, U.; Zheng, X.; Centini, M.; Pfullmann, N.; Herrmann, L. O.; Reinhardt, C.; Volskiy, V.; Silhanek, A. V.; Chichkov, B. N.; Sibilia, C.; Vandenbosch, G. A. E.; Moshchalkov, V. V.; Baumberg, J. J.; Verbiest, T. Nanostripe length dependence of plasmon-induced material deformations. *Opt. Lett.* 2013, *38*, 2256−2258.

(35) Kuznetsov, A. I.; Koch, J.; Chichkov, B. N. Nanostructuring of thin gold films by femtosecond lasers. *Appl. Phys. A: Mater. Sci. Process.* 2009, *94*, 221−230.

(36) Kuznetsov, A. I.; Unger, C.; Koch, J.; Chichkov, B. N. Laser-induced jet formation and droplet ejection from thin metal films. *Appl. Phys. A: Mater. Sci. Process.* 2012, *106*, 479−487.

(37) Valev, V. K.; Silhanek, A. V.; Jeyaram, Y.; Denkova, D.; De Clercq, B.; Petkov, V.; Zheng, X.; Volskiy, V.; Gillijns, W.; Vandenbosch, G. A. E.; Aktsipetrov, O. A.; Ameloot, M.; Moshchalkov, V. V.; Verbiest, T. Hotspot decorations map plasmonic patterns with the resolution of scanning probe techniques. *Phys. Rev. Lett.* 2011, *106*, 226803.

(38) Viarbitskaya, S.; Teulle, A.; Cuche, A.; Sharma, J.; Girard, C.; Dujardin, E.; Arbouet, A. Morphology-induced redistribution of surface plasmon modes in two-dimensional crystalline gold platelets. *Appl. Phys. Lett.* 2013, *103*, 131112.

(39) Teulle, A.; Marty, R.; Viarbitskaya, S.; Arbouet, A.; Dujardin, E.; Girard, C.; Colas des Francs, G. Scanning optical microscopy modeling in nanoplasmonics. *J. Opt. Soc. Am. B* 2012, *29*, 2431−2437.

(40) Ho, J. R.; Grigoropoulos, C. P.; Humphrey, J. A. C. Computational study of heat transfer and gas dynamics in the pulsed laser evaporation of metals. *J. Appl. Phys.* 1995, *78*, 4696−4709.

(41) Habenicht, A.; Olapinski, M.; Burmeister, F.; Leiderer, P.; Boneberg, J. Jumping, nanodroplets. *Science* 2005, *309*, 2043−2045.

(42) Plech, A.; Kotaidis, V.; Lorenc, M.; Boneberg, J. Femtosecond laser near-field ablation from gold nanoparticles. *Nat. Phys.* 2006, *2*, 44−47.

(43) Koch, J.; Korte, F.; Bauer, T.; Fallnich, C.; Ostendorf, A.; Chichkov, B. N. Nanotexturing of gold films by femtosecond laser-induced melt dynamics. *Appl. Phys. A: Mater. Sci. Process.* 2005, *81*, 325−328.

(44) Meshcheryakov, Y. P.; Bulgakova, N. M. Thermoelastic modeling of microbump and nanojet formation on nanosize gold films under femtosecond laser irradiation. *Appl. Phys. A: Mater. Sci. Process.* 2006, *82*, 363−368.

(45) Ivanov, D. S.; Rethfeld, B.; O'Connor, G. M.; Glynn, T. J.; Volkov, A. N.; Zhigilei, L. V. The mechanism of nanobump formation in femtosecond pulse laser nanostructuring of thin metal films. *Appl. Phys. A: Mater. Sci. Process.* 2008, *92*, 791−796.

(46) Emel'yanov, V. I.; Zayarniy, D. A.; Ionin, A. A.; Kiseleva, I. V.; Kudryashov, S. I.; Makarov, S. V.; Nguyen, T. H. T.; Rudenko, A. A. Nanoscale hydrodynamic instability in a molten thin gold film induced by femtosecond laser ablation. *JETP Lett.* 2014, *99*, 518−522.

(47) Lin, Z.; Zhigilei, L. V. Thermal excitation of d band electrons in Au: implications for laser-induced phase transformations - art. no. 62610U. In *High-Power Laser Ablation VI, Pts 1 and 2*; Phipps, C. R., Ed.; 2006; Vol. *6261*, pp U2610−U2610.

(48) Zhang, Y.; Chen, J. K. Melting and resolidification of gold film irradiated by nano- to femtosecond lasers. *Appl. Phys. A: Mater. Sci. Process.* 2007, *88*, 289−297.

(49) Chen, J.; Chen, W.-K.; Tang, J.; Rentzepis, P. M. Time-resolved structural dynamics of thin metal films heated with femtosecond optical pulses. *Proc. Natl. Acad. Sci.* 2011, *108*, 18887−18892.

(50) Palik, D. *Handbook of Optical Constants of Solids*; Academic Press: New York, 1985.

(51) Lin, Z. B.; Zhigilei, L. V. Time-resolved diffraction profiles and atomic dynamics in short-pulse laser-induced structural transformations: Molecular dynamics study. *Phys. Rev. B* 2006, *73*, 184113.

(52) Arbouet, A.; Voisin, C.; Christofilos, D.; Langot, P.; Del Fatti, N.; Vallee, F.; Lerme, J.; Celep, G.; Cottancin, E.; Gaudry, M.; Pellarin, M.; Broyer, M.; Maillard, M.; Pileni, M. P.; Treguer, M. Electron-phonon scattering in metal clusters. *Phys. Rev. Lett.* 2003, *90*.

(53) de Abajo, F. J. G.; Kociak, M. Probing the photonic local density of states with electron energy loss spectroscopy. *Phys. Rev. Lett.* 2008, *100*, 106804.

(54) Gu, L.; Sigle, W.; Koch, C. T.; Oeguet, B.; van Aken, P. A.; Talebi, N.; Vogelgesang, R.; Mu, J.; Wen, X.; Mao, J. Resonant wedge-plasmon modes in single-crystalline gold nanoplatelets. *Phys. Rev. B* 2011, *83*, 195433.

(55) Arbouet, A.; Mlayah, A.; Girard, C.; Colas des Francs, G. Electron energy losses and cathodoluminescence from complex plasmonic nanostructures: spectra, maps and radiation patterns from a generalized field propagator. *New J. Phys.* 2014, *16*, 113012.

(56) Jaegeler-Hoheisel, T.; Cordeiro, J.; Lecarme, O.; Cuche, A.; Girard, C.; Dujardin, E.; Peyrade, D.; Arbouet, A. Plasmonic shaping in gold nanoparticle three-dimensional assemblies. *J. Phys. Chem. C* 2013, *117*, 23126−23132.

(57) Horcas, I.; Fernandez, R.; Gomez-Rodriguez, J. M.; Colchero, J.; Gomez-Herrero, J.; Baro, A. M. WSXM: A software for scanning probe microscopy and a tool for nanotechnology. *Rev. Sci. Instrum.* 2007, *78*, 013705.